Article type : Original Article

Single-cell transcriptomic analysis reveals a hepatic stellate cell-activation roadmap and myofibroblast origin during liver fibrosis

Wu Yang[1,2]*, Hao He[1,2]*, Tongtong Wang[3], Nan Su[1,2], Feng Zhang[4], Kai Jiang[1], Jing Zhu[1,2], Chonghe Zhang[1,2], Kongyan Niu[1], Luyue Wang[2,5], Xiaodong Yuan[6], Nan Liu[1,2], Lingjie Li[4], Wu Wei[2,5], Junhao Hu[1, 2#]

Affiliations:

[1]Interdisciplinary Research Center on Biology and Chemistry, Shanghai Institute of Organic Chemistry, Chinese Academy of Sciences, Shanghai, China

[2]University of Chinese Academy of Sciences, Beijing, China

[3]Laboratory of Translational Nutritional Biology, Department Health Sciences and Technology, Swiss Federal Institute of Technology Zurich, Zurich, Switzerland

[4]Department of Histoembryology, Genetics and Developmental Biology, Shanghai Key Laboratory of Reproductive Medicine, Shanghai JiaoTong University School of Medicine, Shanghai, China

[5]CAS Key Laboratory of Computational Biology, Shanghai Institute of Nutrition and Health, Chinese Academy of Sciences, Shanghai, China

[6]Department of Organ Transplantation Center, Transplant & Immunology Laboratory, the First Affiliated Hospital of USTC, Division of Life Sciences and Medicine, University of Science and Technology of China, Hefei, China

*These authors contributed equally to this work.

[#]Correspondence should be addressed to:

This article has been accepted for publication and undergone full peer review but has not been through the copyediting, typesetting, pagination and proofreading process, which may lead to differences between this version and the Version of Record. Please cite this article as doi: 10.1002/HEP.31987

Dr. Junhao Hu
Interdisciplinary Research Center on Biology and Chemistry
Shanghai Institute of Organic Chemistry
Chinese Academy of Sciences
100 Haike Rd, Pudong District
203201 Shanghai, China
Phone: +86-21-68582261
Email: jhhu@sioc.ac.cn

Word count: 5823 words (excluding references)

Abstract:

Hepatic stellate cells (HSCs) and portal fibroblasts (PFs) are the major sources of collagen-producing myofibroblasts during liver fibrosis, depending on different etiologies. However, the mechanisms by which their dynamic gene expression directs the transition from the quiescent to the activated state—as well as their contributions to fibrotic myofibroblasts—remain unclear. Here, we analyze the activation of HSCs and PFs in CCL_4- and bile duct ligation (BDL)-induced fibrosis mouse models, using single-cell RNA-sequencing and lineage tracing. We demonstrate that HSCs, rather than PFs, undergo dramatic transcriptomic changes, with the sequential activation of inflammatory, migrative, and ECM-producing programs. The data also reveal that HSCs are the exclusive source of myofibroblasts in CCL_4-treated liver, while PFs are the major source of myofibroblasts in early cholestatic liver fibrosis. Single-cell and lineage-tracing analysis also uncovers differential gene expression features between HSCs and PFs; for example, nitric oxide (NO) receptor soluble guanylate cyclase (sGC) is exclusively expressed in HSCs, but not in PFs. The sGC stimulator Riociguat potently reduced liver fibrosis in CCL_4-treated livers but showed no therapeutic efficacy in BDL livers. This study provides a transcriptional roadmap for the activation of HSCs during liver fibrosis and yields comprehensive evidence that the differential transcriptomic features of HSCs and PFs, along with their relative contributions to liver fibrosis of different etiologies, should be considered in developing effective anti-fibrotic therapeutic strategies.

Key words: liver fibrosis, hepatic stellate cell, portal fibroblast, myofibroblast, single-cell RNA sequencing, lineage tracing

One-sentence summary: scRNA-seq elucidates the activation roadmap of HSCs.

Introduction:

Liver fibrosis and liver cirrhosis (the advanced stage of liver fibrosis) are leading causes of morbidity and mortality worldwide (1, 2). Liver fibrosis results from sustained liver injury, which is caused by intrahepatic cholestasis, uncontrolled alcohol consumption, infection with hepatitis viruses, and abnormal metabolic conditions associated with obesity and diabetes. Liver fibrosis is characterized by the emergence of myofibroblasts, which produce excessive extracellular matrix, resulting in the progressive loss of liver microstructure and metabolic function and eventual liver failure (3). However, effective therapeutics to stop or reverse liver fibrosis are not yet available. The growing number of patients with liver fibrosis highlights the urgent need to develop novel mechanistic-based therapies for treating fibrosis.

HSCs, which reside between liver sinusoidal endothelial cells and hepatocytes, are recognized as one of the major origins of myofibroblasts in liver fibrosis of various etiologies (4). Quiescent HSCs store Vitamin A-containing lipid droplets and express specific markers, such as *Desmin* and lecithin retinol acyltransferase (*Lrat*). In response to liver injury, HSCs gradually lose Vitamin A-containing lipid droplets, migrate to the injury sites, and transdifferentiate into myofibroblasts expressing α-SMA and collagen (4). However, the contribution of PFs (which reside in the portal triad) in liver fibrosis remains controversial (5). *Lrat-cre*-based lineage tracing suggests that HSCs give rise to about 90% of myofibroblasts in mouse models of toxic, cholestatic, and fatty liver disease (6), while other studies using *Col-GFP* mice and *MDR2* knockout mice have found that both HSCs and PFs contribute to the myofibroblasts reservoir, with more than 70% of myofibroblasts originating from PFs in early cholestatic fibrosis (7, 8). Previous studies have shown that myofibroblasts originating from HSCs and PFs express different markers (7), although it is unclear whether these myofibroblasts of different origins share similar gene signatures or respond similarly to the same anti-fibrotic therapies.

Single-cell RNA sequencing (scRNA-seq) enables genome-wide gene expression analysis at single-cell resolution, providing unprecedented benefits for identifying cellular heterogeneity, the transition of cellular states, and intercellular communications in complex tissue in health and disease conditions (9). Recent studies using scRNA-seq reveal the emergence of liver parenchymal and non-

parenchymal cells during embryonic development (10), as well as the zonated gene expression patterns of hepatocytes, LSECs, and HSCs in adult mouse livers (11-13). Analysis of human and mouse fibrotic livers with scRNA-seq has uncovered complex intrahepatic communications and the emergence of TREM2+ macrophages (11, 14). While different HSC subsets during activation have been identified (15-17), a detailed roadmap of the transcriptional dynamics of the transition from quiescent HSCs to activated collagen-producing myofibroblasts remains unavailable.

In this study, we perform scRNA-seq to examine the transcriptional dynamics of HSC activation in hepatotoxin-induced and cholestatic liver fibrosis mouse models. Our analysis reveals that, during HSC fibrotic activation, the expression of genes associated with the quiescent state is quickly downregulated, followed by sequential activation of genes involved in the inflammatory response, cell migration, and eventual ECM production. Furthermore, by combining scRNA-seq with lineage tracing, we demonstrate that HSCs are the predominant origin for collagen-producing myofibroblasts in CCL_4-induced liver fibrosis, while PFs are the major source of collagen-producing myofibroblasts in early BDL-induced cholestatic liver fibrosis. Consequently, Riociguat, which activates sGC in HSCs, effectively suppresses liver fibrosis in the CCL_4 model, while it shows no obvious therapeutic effect in the BDL model. Overall, our data suggest that different cell origins and the heterogeneity of profibrotic cells should be accounted for in the development of effective anti-fibrosis treatments.

Materials and methods:

Mice and genotyping

Gucy1a1-CreER^{T2} knock-in mice were generated by inserting a *CreER^{T2}-WPRE-polyA* cassette directly behind the start codon of *Gucy1a1* (Biocytogen Co., Beijing). *Gucy1a1-EGFP* transgenic mice were acquired from GENSAT.org. *Rosa26-LSL-tdTomato* (Stock No. 007900) and *CCL2-RFP^{flox}* (Stock No. 016849) mice were acquired from the Jackson Laboratory. Wild type C57BL/6J mice were purchased from Charles River (Beijing). Only male mice at the age of 8-12 weeks were used in this study. All mice were housed in a barrier SPF facility at the Interdisciplinary Research Center on Biology and Chemistry (IRCBC) with free access to food and water. All animal experiments were performed according to the protocol (IRCBC-2017-002) that was approved by the

Institutional Animal Care and Use Committee (IACUC) of the IRCBC. All genotyping primers are listed in **Supplementary Table 1**.

Liver injury models and Riociguat treatment regimen

To model hepatotoxin-induced liver fibrosis, mice were intraperitoneally injected with carbon tetrachloride (CCL_4, 1 ml/kg body weight and 1:5 diluted in corn oil) twice a week for three weeks. Livers were harvested 24 hours after the final injection. To model cholestatic liver fibrosis, the common bile duct was ligated under isoflurane anesthesia. The livers were harvested ten days after the operation. Livers were harvest 24 hours after the second injection. For treatment, mice received Riociguat (Selleck, S8135, 10 mg/kg body weight) or vehicle control twice a day via oral gavage.

Cell isolation

Liver non-parenchymal cells were isolated following a two-step perfusion protocol as previously described (18). The livers were briefly perfused *in situ* with 37˚C EGTA solution, followed by sequential perfusion with Pronase E (0.4 mg/mL, Merck Millipore, 1.07433.0005) for 5 minutes and Collagenase IV (0.48 mg/mL, Sigma-Aldrich, C5138) for 7 minutes. Next, the livers were dissected and transferred into 50-ml falcon tubes and further digested with buffer containing 0.5 mg/mL Pronase E, 0.5 mg/mL Collagenase IV, and 0.02 mg/mL DNase I (Roche, 10104159001) in a 37°C water bath with gentle agitation for 25 minutes. Digested livers were passed through a 70-μm cell strainer and centrifuged at 580 g for 10 minutes. The liver cells were washed twice with GBSS/B buffer and resuspended in 32 mL GBSS/B buffer. Finally, the liver cells were subjected to density gradient separation with 9.69% Nycodenz (Histodenz) solution (Sigma-Aldrich, cat. no. D2158) and centrifuged at 1,380g for 17 minutes at 4˚C without brake to enrich liver non-parenchymal cells. Cell viability (>90%) was determined using trypan blue staining.

Single-cell RNA sequencing and data analysis

The liver non-parenchymal cells of three mice per group were pooled and loaded into the 10x Genomics Chromium Single Cell chips. Libraries were prepared using the Chromium Single Cell 3' GEM Library & Gel Bead Kit v3 (10X Genomics, cat. no. PN-1000075) according to the

manufacturer's instructions, and sequenced on an Illumina Novaseq. Sequencing data were processed with Seurat (v3) single-cell analysis pipeline with modifications. Pseudotime trajectory was inferred using Slingshot. (For more details, see Supplementary materials)

Histology and immunohistochemistry

Paraffin-embedded PFA-fixed livers sections were stained with Sirius Red. For immunofluorescent staining, all liver samples were fixed with PFA and cryopreserved in OCT. Following primary antibodies were used in this study: Anti-Desmin antibody (Abcam, Ab15200-1), anti-CD31 antibody (Thermo Fisher, MA3105), anti-GUCY1A1 antibody (Proteintech, 12605-1-AP), anti-aSMA antibody (Sigma, C6198), anti-THY1 antibody (Biolegend, 105302), anti-COLLAGEN 1 antibody (BioRad, 2150-1410), anti-MCP1 antibody (Proteintech, 66272-1-lg), anti-Ki67 antibody (Abcam, ab16667), and anti-CD45 antibody (Proteintech, 20103-1-AP). (For more details, see Supplementary materials)

Statistical analysis

All statistical analyses were performed using GraphPad Prism (v8) or functions in R/Bioconductor packages. Student's t-test was performed for two-group comparison, and one-way ANOVA with Tukey HSD post-hoc test was performed for multiple-group comparison. Differences between groups were considered to be significant at a P-value <0.05. All data are presented as mean ± SD unless specifically explained.

Results:

Single-cell RNA sequencing analysis of nonparenchymal hepatic cells

To understand HSC activation during liver fibrosis, we performed a droplet-based single-cell transcriptomic analysis (10X Chromium). Because liver fibrosis can occur in the pericentral or periportal regions due to different etiologies, we adopted two different experimental models—the intraperitoneal CCL_4 injection-induced hepatotoxic fibrosis model and the bile duct ligation-induced cholestatic fibrosis model—to induce pericentral and periportal injury, respectively **(Figure 1A)**. We isolated HSCs from the livers of oil-treated control, CCL_4-treated, or bile duct-ligated mice, using sequential pronase-collagenase digestion and the Nycodenz gradient separation protocol; we then

performed single-cell RNA sequencing (6). After quality filtering, 47,752 cells (10,636 cells from oil control, 18,185 cells from CCL_4-treated, and 18,931 cells from BDL mice), with an average sequencing depth of 2353 genes per cell, were subjected to further analysis. Unsupervised clustering classified these cells into eight distinct clusters with HSCs as the largest cell cluster. **(Figure 1B, C and Supplementary Figure 1A, B)**. The other cell clusters were classified as ECs, Kupffer cells, PFs, leukocytes, hepatocytes, and cholangiocytes, based on the expression of cell type-specific marker genes **(Figure 1B-D)**. Interestingly, we found that cholangiocytes were divided into two clusters—*Sox9*+ cholangiocytes and *Sox9*- cholangiocytes **(Figure 1B-D)**—which aligns with Tulasi's finding based on SOX9 immunofluorescent staining, reflecting the heterogeneity of their intrahepatic localization and regeneration capacity (19).

HSCs represent the largest cell clusters, accounting for about 60% of total cells analyzed in this study **(Supplementary Figure 1A)**. Interestingly, we observe a dramatic shift of the HSC clusters from the livers with CCL_4 treatment or bile duct ligation towards the PF clusters, while the HSC cluster of the control mouse was distinctly separated from the PFs **(Figure 1B)**. In contrast, this transcriptomic shift was not observed in PFs, which undergo marked expansion in BDL livers, indicating that HSCs and PFs undergo different activation mechanisms during liver fibrosis.

Single-cell RNA-seq provides tremendous power in identifying novel cell-type-specific genes (9, 20). In addition to the well-known HSC markers *Desmin*, *Lrat*, and *Pdgfrb*, our single-cell analysis revealed specific expression of *Rgs5*, *Reln*, *Pth1r*, *Tmem56*, *Vipr1*, *Angptl6*, and *Fcna* in HSCs **(Supplementary figure 1B)**, similar to other recently published single-cell studies on HSCs (11, 14, 17, 21). Interestingly, our study found that *Gucy1a1* and *Gucy1b1*, which are the α1 and β1 subunits of the nitric oxide (NO) receptor soluble guanylate cyclase (sGC), was highly expressed in HSCs **(Figure 1E)**. To validate the expression specificity of *Gucy1a1* and *Gucy1b1*, we isolated different hepatic cells, including hepatocytes, LSECS, Kupffer cells, and HSCs, and performed bulk RNA-seq and qPCR analysis. Indeed, the expression of *Gucy1a1* and *Gucy1b1* was detected only in HSCs, but not in other hepatic cell populations **(Supplementary Figure 2A-B)**. We further confirmed the expression of sGC in the liver using a GUCY1A1 antibody and *Gucy1a1-EGFP* reporter mice.

Immunofluorescent staining shows that the GUCY1A1 antibody completely colocalized with the EGFP signal, indicating that EGFP expression faithfully reflected the endogenous *Gucy1a1* expression **(Supplementary Figure 2C)**. Additional immunostaining and three-dimensional reconstruction revealed that EGFP was colocalized with the HSC-specific Desmin-positive cells, and that EGFP+ cells showed typical HSC morphology, with extended cytoplasmic processes wrapping the sinusoidal endothelium **(Figure 1F, Supplementary Figure 2D-F)**. Flow cytometry analysis demonstrates that EGFP-labeled cells were positive for Vitamin-A-containing lipid droplets, a unique feature of HSCs, further substantiating their HSC identity **(Supplementary Figure 2G)**.

Gene expression dynamics define HSC stages during fibrotic activation

To elucidate HSC activation during liver fibrosis, we extracted transcriptomic information on all HSCs for further analysis. UMAP visualization showed that HSCs could be divided into two distinct clusters: quiescent HSCs (qHSCs) and active HSCs (aHSCs) **(Figure 2A)**. In accordance with the established dogma that activated HSCs upregulate migration and extracellular matrix-associated genes during liver fibrosis (4), the aHSCs from both the CCL_4- and BDL- livers showed increased *Acta2*, *Tagln*, *Col1a1*, *Col1a2*, and *Timp1* expression **(Figure 2B-C)**. On the contrary, a group of genes including *Lrat* and *Rgs5*, *Ecm1*, *Angptl6*, *Vipr1, Gucy1a1,* and *Gucy1b1*—which were highly expressed in quiescent HSCs—were markedly downregulated in activated HSCs **(Figure 2B-C)**; this indicates that a dramatic transcriptional reprogramming occurs during HSC activation.

To understand the transcriptional dynamics of HSCs during activation, we reconstructed the gene expression dynamics of HSC activation using Slingshot; we identified four distinct gene expression modules along a single pseudotime trajectory **(Figure 2D-E)**. Genes of the first module were highly expressed in qHSC, with their expression decreasing immediately upon HSC activation. Interestingly, we found that the first module contained well-known HSC markers, such as *Lrat1* and *Rgs5*, as well as genes that are associated with vascular tone and relaxation, such as *Gucy1a1*, *Gucy1b1*, and *Vipr1*. This indicates that HSCs not only quickly lose their quiescent identity but also lose their vascular relaxation capacity, contributing to the increase in intrahepatic vascular resistance and the development of portal hypertension during liver fibrosis **(Cluster-1 of Figure 2E)**. The genes of the

second module were transiently upregulated at the early stages but decreased rapidly afterwards. The majority of genes of the second module encode for inflammatory cytokines, such as *Ccl2* and *Cxcl10*, that are involved in cytokine- chemokine-mediated signaling pathways and leukocyte recruitment **(Cluster-2 of Figure 2E)**. The third module contains genes such as *Acta2*, *Tagln*, and other cell migration and contractility-associated genes; their expression levels slowly increased, reaching their peaks at mid-stage, followed by a mild decrease at the end stage during liver fibrosis **(Cluster-3 of Figure 2E)**. The fourth module, which mainly encompasses genes associated with ECM components such as *Col1a1* and *Col1a2*, exhibited delayed upregulation and reached their peaks at the end stage during HSC activation **(Cluster-4 of Figure 2E)**.

To analyze whether aHSCs could be further divided into different subclusters, we integrated the differential gene expression patterns and the relative spatial distribution of the HSCs along the pseudotime trajectory **(Supplementary Figure 3)**. Based on the different gene expression kinetics of the four gene clusters, we divided aHSCs into three distinct subclusters, defined as stage-1 aHSCs, stage-2 aHSCs, and stage-3 aHSCs **(Figure 3A)**. In line with the four dynamic gene expression modules, a heatmap of the highly expressed genes of each HSC subcluster—as well as GO analysis—demonstrated that stage-1 aHSCs expressed high levels of inflammatory cytokines, including *Ccl2*, *Cxcl10*, and *Ccl7*. Stage-2 aHSCs demonstrated the expression of cell mobility and contractility-associated genes such as *Acta2*, *Tpm1*, *Vim*, *Tagln*, and *Tnc*. Stage-3 aHSCs expressed extremely high levels of ECM deposition and organization-related genes, including *Col1a1*, *Lox*, and *Lum* **(Figure 3B-C)**. Because activated HSCs undergo proliferation to expand the collagen-producing cell reservoir during liver fibrosis, we analyzed aHSC proliferation based on the expression of proliferation markers *Mki67* and *Mcm6*. Overlay of the *Mki67*- and *Mcm6*-expressing cells with an HSC UMAP indicated that only a small fraction of aHSCs underwent proliferation, with most of them being stage-2 aHSCs **(Figure 3D)**.

We further compared the difference in HSC activation in fibrotic livers induced by either CCL_4 or BDL. UMAP projection of HSCs from individual livers indicates that aHSCs of the CCL_4-treated liver showed a different activation pattern than aHSCs from BDL liver. The majority of aHSCs in

CCL_4-treated liver were stage-2 aHSCs and stage-3 aHSCs, accounting for 38.1% and 43.2% of total HSCs, respectively. On the contrary, the majority of aHSCs in BDL liver were stage-1 aHSCs (44.5%), while stage-2 and stage-3 aHSCs only accounted for 11.3% and 11.0%, respectively, of total HSCs in BDL liver **(Figure 3E)**. This result suggests that, unlike the widespread activation of HSCs in the CCL_4 model, HSCs are less activated in the BDL liver at day 10, probably due to the confined portal injury in BDL livers.

To systematically delineate the gene regulatory networks that control HSC homeostasis and activation, we subjected the transcriptomes of the HSCs to unbiased single-cell regulatory networks inference and clustering (SCENIC) analysis (22, 23). We identified 284 orthologous transcription factors grouped into four regulatory modules, indicating differential transcription factor activity during HSC activation. Consistent with previous studies based on HSC-specific gene deletion (24, 25), SCENIC analysis showed that transcription factors of the *Ets* family, *Gata* family, *Irf1, Irf2, Foxo1,* and *Ppar* family were involved in maintaining the HSC quiescent status. Notably, as with the gene expression patterns in HSCs at different stages **(Supplementary Figure 4A-B)**, *Nfkb1/2*, *Relb*, and *Stat2/3* were involved in controlling inflammatory gene expression in HSCs at stage-1; the *SRF*, *Jun*, and *Fos* transcription factors were responsible for the enhanced cell migration phenotype, while *Wt1* and *Runx1* participated in increased collagen deposition (26). Interestingly, SCENIC analysis also identified transcription factors not previously implicated in controlling HSC function, such as *Hey2* and *Trp53*—which may play roles in maintaining HSC quiescence—as well as *Atf3/6*, and *Meis1/2*, which may be involved in regulating HSC activation.

The morphological dynamics of HSCs during fibrotic activation

It has been shown that, along with the dramatic changes in gene expression during *in vitro* activation, HSCs lose their unique stellate shape and acquire a distinct spindle-like myofibroblast morphology (27). However, it is unclear whether this morphological change is associated with HSC activation *in vivo*. To investigate, we utilized *Gucy1a1-EGFP* mice to track the change in HSC morphology. *Gucy1a1-EGFP* mice were treated with CCL_4 or BDL to induce liver fibrosis. Next, the whole liver sections of control, CCL_4-treated, and BDL-treated *Gucy1a1-EGFP* mice were scanned in z-stack

mode using spinning disk confocal microscopy. The morphology of EGFP-positive HSCs was first 3D-reconstructed, followed by skeletonization to show the cell body and cytoplasmic processes. The analysis demonstrated that HSCs of CCL_4-treated livers showed a marked reduction in total filament volume, branch numbers per cell, total branch length per cell, and mean branch length per cell, compared to HSCs from the control liver **(Figure 4A-B)**. On the contrary, HSCs from BDL livers showed a reduced branch number per cell compared to HSCs from control livers; their total filament volume, branch number per cell, total branch length, and mean branch length per cell were still significantly higher than in HSCs from CCL_4-treated livers. This result indicates that HSCs are more activated in CCL_4-treated liver than in BDL-treated liver, which aligns with the results of the transcriptomic-based single-cell analysis, which shows that the majority of aHSCs in CCL_4-treated livers were at stage 2 and stage 3, while most aHSCs in BDL liver were at stage 1 **(Figure 3E)**.

We next examined whether aHSCs at different activated stages have distinct morphological features. To this aim, we characterized the morphology of quiescent HSCs from the livers of control *Gucy1a1-EGFP* mice to serve as a reference **(Figure 4C, 1st-2nd row)**. To identify aHSCs at different stages, we first defined the terminally activated collagen-producing stage-3 aHSCs in the liver sections of CCL_4-treated *Gucy1a1-EGFP* mice, based on their collagen-1 expression. Next, we defined stage-1 and stage-2 aHSCs based on their relative distance to stage-3 aHSCs **(Figure 4C, 3rd-6th row)**. While the results show that the stage-1 aHSCs still maintained a stellate morphology similar to qHSCs, stage-2 and stage-3 aHSCs acquired a spindle-like morphology with reduced cell volume and branch counts **(Figure 4C-D)**. Nevertheless, HSCs (even those adjacent to the collagen-positive fibrotic scar) in the BDL livers still maintained a stellate morphology, indicating that the majority of HSCs were not terminally transdifferentiated into myofibroblasts in the livers ten days after bile duct ligation **(Supplementary Figure 5)**.

Portal fibroblasts—not HSCs—are the major source of collagen-producing cells in cholestatic liver fibrosis

Both HSCs and PFs are activated during cholestatic liver fibrosis (5); however, their contributions to collagen-producing myofibroblasts in cholestatic liver fibrosis remain controversial (6-8). In this

study, we found that the low percentage of collagen-producing stage-3 aHSCs in the BDL liver **(Figure 3E)** could not explain the massive collagen deposition in the portal area **(Supplementary Figure 6)**, suggesting that the collagen in the BDL liver may be deposited primarily by PFs. Therefore, we compared the single-cell transcriptomes of PFs and HSCs, finding that the gene expression patterns of PFs closely resembled those of stage-3 aHSCs **(Figure 5A)**. Nevertheless, PFs could be easily distinguished from stage-3 aHSCs in two-dimensional and three-dimensional UMAP presentations, due to the expression of PF-specific makers, including *Thy1*, *Fbln1*, *Eln*, *Dpt*, *Mfap4*, and *Gas6*, **(Figure1B-C, Figure 5B-C)**. Furthermore, the PFs of CCL_4-treated liver expressed similar levels of *Col1a1* and *Col1a2* compared to aHSCs, while the PFs of BDL liver expressed significantly higher levels of *Col1a1* and *Col1a2* than aHSCs **(Figure 5C)**, indicating that PFs are the principal collagen-producing cells in cholestatic liver fibrosis. As in previous studies (28), the percentage of PFs was very low in the healthy liver **(Figure 5D)**. The number of PFs was increased in the CCL_4-treated liver. However, the number of PFs was dramatically elevated in the BDL liver—a fifty-seven-fold increase compared to the number of PFs in healthy liver and a twelve-fold increase compared to the number of PFs in CCL_4-treated livers **(Figure 5D-F).**

We further verified the contribution of HSCs and PFs to collagen-producing myofibroblasts in CCL_4- and BDL-induced liver fibrosis, using *Gucy1a1-EGFP* mice. Confocal imaging analysis demonstrate that, in the CCL_4-treated liver, the majority of the collagen-producing cells were derived from HSCs, as they were EGFP-positive. On the contrary, the collagen-producing cells in the BDL liver were negative for EGFP but positive for the PF marker *Thy1* **(Figure 6A)**. Notably, our analysis showed that the expression of *Gucy1a1* and *Gucy1b1* declined during HSC activation **(Figure 2F)**. Thus, to exclude the possibility that a dramatic reduction in EGFP expression occurred in terminally activated HSCs—and to precisely determine the contribution of HSCs to the collagen-producing myofibroblasts in cholestatic liver fibrosis—we generated *Gucy1a1-CreER^{T2}* mice to permanently label HSCs during liver fibrosis **(Supplementary Figure 7A)**. We crossed *Gucy1a1-EGFP* with *Gucy1a1-CreERT2* and *Rosa26-LSL-tdTomato* mice; we injected five doses of Tamoxifen at the age of 4 weeks and determined the labeling efficiency at the age of 8 weeks. Immunofluorescent imaging and flow cytometry analysis revealed that approximately 90% of EGFP+ HSCs were labeled with permanently

expressed tdTomato upon Tamoxifen induction **(Supplementary Figure 7B-C)**. Next, we performed bile duct ligation to induce cholestatic liver fibrosis in *Gucy1a1-EGFP::Gucy1a1-CreERT2::Rosa26-LSL-tdTomato* mice at the age of 8 weeks. Lineage tracing results showed that the collagen-positive cells in the BDL liver were predominantly positive for *Thy1* but negative for both EGFP and tdTomato **(Figure 6B-C)**. Therefore, the lineage tracing data and scRNA-seq analysis demonstrate that, during cholestatic liver injury, PFs (which are activated and undergo dramatic expansion) are the major source of collagen deposition, while HSCs make a minimal contribution to the excessive collagen deposition.

Activating sGC inhibits HSC activation and ameliorates hepatotoxin-induced liver fibrosis, but not cholestatic liver fibrosis

Several studies have shown that sCG-activating reagents inhibit liver fibrosis in different preclinical rodent models of pig serum, CCL_4 treatment, and high-fat-diet-induced NASH, or BDL (29-32). In this study, we found that expression of sGC subunits *Gucy1a1* and *Gucy1b1* were decreased upon HSC activation, with the lowest expression levels in stage-3 aHSCs **(Figure 2F, Figure 7A-B).** More importantly, our data show that collagen-producing cells in BDL model originated primarily from PFs, which did not express sGC **(Figure 6A-B)**. These results prompted us to re-evaluate the therapeutic effects of sGC activation in CCL_4- and BDL-induced liver fibrosis models. Considering that later-stage activated HSCs may impede their response to sGC-activating reagents due to the reduction of sGC expression, Riociguat, an sGC stimulator that has been FDA-approved for treating pulmonary arterial hypertension (33), was administered one day after bile duct ligation or the first dose of CCL_4 **(Figure 7C)**. The analysis shows that Riociguat treatment significantly reduced collagen deposition in CCL_4-treated livers, as evidenced by Sirius red staining **(Figure 7C-D)**. The reduction in collagen deposition upon Riociguat treatment was further confirmed by a remarkable decrease in the hydroxyproline content in the liver **(Figure 7D)**. Furthermore, Riociguat treatment also reduced ALT and AST levels in the serum, indicating that activating sGC protected the liver from CCL_4-induced liver injury **(Figure 7D)**. On the contrary, Riociguat did not reduce liver fibrosis and liver injury in BDL mice at day 10 **(Figure 7E-F)**. This data substantiating the notion that sGC-activating agents should only be used to combat liver fibrosis that activated HSCs, which express sGC, are the

predominant source of collagen deposition, but not cholestatic liver fibrosis, in which PFs are the major source of accumulated collagen.

To gain further insight into the mechanisms by which sGC activation inhibits HSCs activation, we stimulated isolated mouse HSCs with Riociguat and performed bulk transcriptomic analysis, which provides higher sequencing depth than single-cell RNA-sequencing. Riociguat treatment significantly elevated cGMP concentration in cultured HSCs **(Supplementary Figure 8A)**. Transcriptomic profiling reveals that Riociguat treatment markedly suppressed the expression of 822 genes in HSCs **(Supplementary Figure 8B)**. Gene set enrichment analysis (GSEA) indicates that Riociguat treatment potently inhibited gene expression related to cell migration and actin cytoskeleton rearrangement, inflammatory cytokines response, and collagen production **(Supplementary Figure 8C-F)**. Interestingly, we also identified a small set of genes belonging to the Hippo pathway—including *Ankrd1*, *Cyr61*, *Ctgf*, and *Thbs1*—which were also significantly suppressed by Riociguat treatment **(Supplementary Figure 8G-H)**. This accords with a previous finding that inhibition of YAP impedes liver fibrosis (34). These results suggest that activating sGC could potently inhibit the expression of inflammatory cytokines, as well as HSC migration, thereby blocking HSC activation at early stages and preventing HSCs from differentiating into later-stage collagen-producing myofibroblasts.

Discussion:

Chronic fibrosis caused by various etiologies, including sustained hepatitis virus infection and alcoholic and nonalcoholic liver diseases, is a global healthcare burden, with total mortality of two million deaths per year (1). Many strategies targeting TGFβ, PDGF, CTGF, LXR, and NOX have been developed to inhibit the differentiation and proliferation of collagen-producing myofibroblasts. However, their clinical deployment has achieved limited success, and no effective anti-fibrosis treatment options are yet available. Hence, it is crucial to improve our understanding of the molecular mechanisms underlying liver fibrosis and to translate that knowledge into better mechanistic-based therapeutic strategies. In this study, we describe the HSC activation program and evaluate the origins of collagen-producing myofibroblasts in CCL_4- and BDL-induced fibrotic livers, using single-cell

transcriptomic analysis and lineage-tracing strategies. We also uncover that myofibroblasts of different-origins respond differently to anti-fibrotic therapy.

Cellular heterogeneity within individual cell types—including hepatocytes, LSECs, and HSCs—in healthy livers has recently been investigated using single-cell analysis. Similar to hepatocytes, HSCs also demonstrate zonated gene expression patters, with periportal HSCs expressing *Ngfr* and *Igfbp3* and pericentral HSCs expressing *Adamtsl2* and *Loxl1* (21). Single-cell analysis of HSCs from various fibrosis mouse models reveals that quiescent and activated HSCs displayed distinct gene expression profiles. In line with previous findings using bulk-RNA-seq, single cell analysis data from our study and others consistently show that aHSCs profoundly upregulate migration and ECM-associated genes such as *Col1a1* and *Acta2* (14, 21). Furthermore, heterogeneity within aHSCs in fibrotic liver has also been recently reported. Rosenthal et al. show that aHSCs in NASH livers can be further divided into a proliferating cluster, an intermediate activated cluster, an immune and inflammatory cluster, and a classic fibrogenic myofibroblast cluster (17).

aHSCs are known to be inflammatory, chemotactic, migrative, contractile, and characterized by increased collagen production (4). However, it is unknown whether HSCs acquire these profibrotic features in a simultaneous or sequential manner during activation. Using scRNA-seq and pseudotime trajectory, we infer a roadmap of cell-state transition from qHSCs to terminally differentiated collagen-producing aHSCs during liver fibrosis. Upon fibrotic insult, qHSCs sequentially differentiate into stage-1 aHSCs with an inflammatory gene signature. Subsequently, they progress into stage-2 aHSCs with a migrative and contractile gene signature and, eventually, into ECM-producing stage-3 aHSCs. Thus, the analysis indicates that HSC activation follows a sequential activation model orchestrated by waves of gene expression; this requires inactivation of the gene signature of the current stage before the initiation of the gene signature of next stage. Interestingly, this sequential activation has also been observed in HSCs undergoing *in vitro* activation (15). Another surprising finding is that—in contrast to HSCs, which undergo the dramatic transcriptomic shift during activation—PFs undergo dramatic expansion, especially in the BDL livers, as evidenced by the

single-cell and histological analysis, although they did not exhibit transcriptomic changes during liver fibrosis.

While HSCs from CCL_4-treated and BDL-treated livers follow the same activation trajectory, the percentage of aHSCs and the compositions of different subclusters in CCL_4-treated and BDL livers are quite different. Our scRNA-seq reveals that HSCs in CCL_4-treated liver were highly activated, with the elevated ECM produced by stage-3 aHSCs. By contrast, the HSCs in BDL liver are less activated, as evidenced by the fact that the dominant subcluster was stage-1 aHSCs. Meanwhile, the number of PFs was dramatically expanded in BDL liver. We further generated *Gucy1a1-CreER^{T2}* mice—which are the first HSC-specific conditional Cre mice—to trace the origin of myofibroblasts in fibrotic livers. Analysis of the livers of *Gucy1a1-CreER^{T2}::Rosa26-LSL-tdTomato* mice shows that the predominant myofibroblasts in BDL livers were tdTomato-negative but *Thy1*-positive, while the collagen-producing myofibroblasts in CCL_4-treated liver were tdTomato-positive, suggesting that the dominant origin of myofibroblasts in cholestatic liver injury is PFs. Our observations align with those of previous studies that used *Col-GFP* and *Mdr2* knockout mice (7, 8); our findings contradict those of a previous study based on Lrat-Cre, which found that myofibroblasts in BDL liver have an HSC origin (6). The discrepancy possibly stems from the fact that, in addition to HSCs, the constitutive *Lrat-Cre* may also label some PFs during embryonic development, as they share the same mesenchymal origin. Notably, our analyses were performed 10 days after BDL, which only reflects the early or intermediate stage of cholestatic injury. The contribution of HSCs to myofibroblasts in cholestatic liver injury would increase in late-stage cholestatic models, as Iwaisako *et al.* demonstrated that the number of aHSCs and the expression of *Col1a1* in livers are higher 20 days after BDL than 5 days after BDL (7).

Single-cell RNA sequencing shows remarkable power in discovering new cell-type specific makers. In this study, unsupervised single-cell analysis showed that *Lrat*, *Vipr1*, *Ecm1*, *Gucy1a1*, and *Gucy1b1* were highly and specifically expressed in HSCs. In particular, their expression levels are associated with the maintenance of the quiescent state in HSCs. Among these genes are *Gucy1a1* and *Gucy1b1*, which are the α1 and β1 subunits of the NO receptor sGC (33). scRNA-seq data and

Gucy1a1-CreER^{T2}::Rosa26-LSL-tdTomato lineage-tracing show that sGC (*Gucy1a1*/*Gucy1b1*) is specifically expressed in HSCs and in HSC-derived myofibroblasts, but not in *Thy1*-positive PFs and PF-derived myofibroblasts. Furthermore, a steady decrease in *Gucy1a1* and *Gucy1b1* expression in aHSC was observed, which would lead to impaired HSC relaxation and the onset of portal hypertension. Preclinical evidence shows that the activation of sGC can inhibit liver fibrosis in mouse models induced with pig serum, CCL_4, or diet (29, 31, 32). Another study reports that the sGC stimulator Riociguat reduces portal pressure and liver fibrosis in both CCL_4 and BDL rat models (30). However, in our study, Riociguat treatment potently inhibited liver fibrosis in CCL_4-treated mice, but not in the BDL mouse model. The discrepancy may stem from the different experimental designs as we performed BDL in mice and analyzed the liver 10 days after operation, while Schwabl *et al.* performed BDL in rats and analyzed the livers 3 weeks and 5 weeks after operation, as previous study by Iwaisako demonstrates that the contribution of HSCs to collagen-producing myofibroblasts increases over time after BDL (7). Therefore, it is reasonable to expect that a substantial proportion of sGC-expressing HSCs may be differentiate into stage-3 HSCs in cholestatic livers 3 or 5 weeks after BDL and, thus, the administration of the sGC stimulator Riociguat under such conditions may exhibit anti-fibrosis effect. Nonetheless, our study suggests that the differences between collagen-producing myofibroblasts of different origins in fibrotic livers should be further investigated and taken into account for designing better anti-fibrotic therapy strategies in the future.

In fibrotic liver, aHSCs are extensively heterogeneous, with terminally activated aHSCs located at the fibrotic center, where the liver injury happens, and less-activated aHSCs located away from the fibrotic center. This poses a significant challenge for effective anti-fibrotic treatment, because most therapies under development are single-agent treatments that target only one subcluster of aHSCs, therefore, they are not able to effectively stop the progression of liver fibrosis. Currently, many agents targeting specific gene and fibrotic signaling pathways have been developed and tested in various clinical trials. The CCL2-inhibitor Bindarit (35) and the CCR2-antagnisot RS-504393 (36) block CCL2 secreted by stage-1 aHSCs; the Rock-inhibitor Y-27632 (37) and the FAK-inhibitors PF-562271 (38) impede the migration of stage-2 aHSCs; and LOXL2-neutralizing antibody interferes in the organization of ECM secreted by stage-3 aHSCs (39). However, the clinical deployment of these

agents as single-agent therapies has had limited success. Therefore, a combination of agents to target multiple subclusters of aHSCs may provide better clinical outcomes in treating liver fibrosis.

In summary, by employing scRNA-seq with different preclinical fibrosis mouse models, we provide a detailed transcriptional roadmap of HSC activation that is shared by both CCL_4- and BDL-induced liver fibrosis. Upon fibrotic activation, HSCs sequentially acquire inflammatory, migrative, and contractile phenotypes, before eventually differentiating into collagen-producing myofibroblasts. We also demonstrate that HSCs minimally contribute to collagen-producing fibroblasts in the early phase of BDL-induced liver fibrosis, which leads to the differential therapeutic outcome of HSC-targeting Riociguat treatment. Our discovery provides important insight into the mechanisms of HSC activation, heterogeneity, and differential cellular-source myofibroblasts during liver fibrosis. Our findings potentially open avenues for developing better therapeutic strategies for the treatment of liver fibrosis.

Author contribution: WY prepared fibrosis mouse models and performed therapeutic treatment. WY, KN, and NL performed 10X single-cell library preparation. HH, WY, TW, FZ, LW, LL, WW, and JH analyzed the single-cell data. HH and WY analyzed the bulk RNA-seq data. WY, JZ, NS, KJ, XY, CZ, and XY contributed to tissue collection, and histology analysis. WY, HH, and JH designed the study and wrote the manuscript.

Acknowledgements:

We gratefully acknowledge Dr. Mahak Singhal (German Cancer Research Center) for critical suggestions, Dr. Yang Geng of the microscopy facility and Junda Ni, Teng Geng, and Zhengqiang Qi of laboratory animal core facility for excellent support.

Data and materials availability: All sequencing data are deposited in the Gene Expression Omnibus (GEO) with the accession number GSE171904 (single-cell transcriptomic profiling), and GSE171885 (bulk transcriptomic analysis of Riociguat-treated HSCs).

Financial support: This work was supported by the National Science Foundation of China (NFSC) (No. 31872797 and No. 92042304), and the Shanghai Municipal Science and Technology Major Project (No. 2019SHZDZX02).

Conflict of interest: The authors declare no conflict of interest.

References:

1. Marcellin P, Kutala BK. Liver diseases: A major, neglected global public health problem requiring urgent actions and large-scale screening. Liver Int 2018;38 Suppl 1:2-6.
2. **Asrani SK, Devarbhavi H,** Eaton J, Kamath PS. Burden of liver diseases in the world. J Hepatol 2019;70:151-171.
3. Hernandez-Gea V, Friedman SL. Pathogenesis of liver fibrosis. Annu Rev Pathol 2011;6:425-456.
4. Tsuchida T, Friedman SL. Mechanisms of hepatic stellate cell activation. Nat Rev Gastroenterol Hepatol 2017;14:397-411.
5. Kisseleva T. The origin of fibrogenic myofibroblasts in fibrotic liver. Hepatology 2017;65:1039-1043.
6. Mederacke I, Hsu CC, Troeger JS, Huebener P, Mu X, Dapito DH, Pradere JP, et al. Fate tracing reveals hepatic stellate cells as dominant contributors to liver fibrosis independent of its aetiology. Nat Commun 2013;4:2823.
7. **Iwaisako K, Jiang C, Zhang M,** Cong M, Moore-Morris TJ, Park TJ, Liu X, et al. Origin of myofibroblasts in the fibrotic liver in mice. Proc Natl Acad Sci U S A 2014;111:E3297-3305.
8. Nishio T, Hu R, Koyama Y, Liang S, Rosenthal SB, Yamamoto G, Karin D, et al. Activated hepatic stellate cells and portal fibroblasts contribute to cholestatic liver fibrosis in MDR2 knockout mice. J Hepatol 2019;71:573-585.

9. Ramachandran P, Matchett KP, Dobie R, Wilson-Kanamori JR, Henderson NC. Single-cell technologies in hepatology: new insights into liver biology and disease pathogenesis. Nat Rev Gastroenterol Hepatol 2020;17:457-472.

10. Lotto J, Drissler S, Cullum R, Wei W, Setty M, Bell EM, Boutet SC, et al. Single-Cell Transcriptomics Reveals Early Emergence of Liver Parenchymal and Non-parenchymal Cell Lineages. Cell 2020;183:702-716 e714.

11. Ramachandran P, Dobie R, Wilson-Kanamori JR, Dora EF, Henderson BEP, Luu NT, Portman JR, et al. Resolving the fibrotic niche of human liver cirrhosis at single-cell level. Nature 2019;575:512-518.

12. **Halpern KB, Shenhav R,** Massalha H, Toth B, Egozi A, Massasa EE, Medgalia C, et al. Paired-cell sequencing enables spatial gene expression mapping of liver endothelial cells. Nat Biotechnol 2018;36:962-970.

13. **Halpern KB, Shenhav R,** Matcovitch-Natan O, Toth B, Lemze D, Golan M, Massasa EE, et al. Single-cell spatial reconstruction reveals global division of labour in the mammalian liver. Nature 2017;542:352-356.

14. **Xiong X, Kuang H, Ansari S, Liu T,** Gong J, Wang S, Zhao XY, et al. Landscape of Intercellular Crosstalk in Healthy and NASH Liver Revealed by Single-Cell Secretome Gene Analysis. Mol Cell 2019;75:644-660 e645.

15. Krenkel O, Hundertmark J, Ritz TP, Weiskirchen R, Tacke F. Single Cell RNA Sequencing Identifies Subsets of Hepatic Stellate Cells and Myofibroblasts in Liver Fibrosis. Cells 2019;8.

16. Terkelsen MK, Bendixen SM, Hansen D, Scott EAH, Moeller AF, Nielsen R, Mandrup S, et al. Transcriptional dynamics of hepatic sinusoid-associated cells after liver injury. Hepatology 2020.

17. Rosenthal SB, Liu X, Ganguly S, Dhar D, Pasillas MP, Ricciardelli E, Li RZ, et al. Heterogeneity of hepatic stellate cells in a mouse model of non-alcoholic steatohepatitis (NASH). Hepatology 2021.

18. **Mederacke I, Dapito DH,** Affo S, Uchinami H, Schwabe RF. High-yield and high-purity isolation of hepatic stellate cells from normal and fibrotic mouse livers. Nat Protoc 2015;10:305-315.

19. Tulasi DY, Castaneda DM, Wager K, Hogan CB, Alcedo KP, Raab JR, Gracz AD. Sox9(EGFP) defines biliary epithelial heterogeneity downstream of Yap activity. Cell Mol Gastroenterol Hepatol 2021.

20. Gawad C, Koh W, Quake SR. Single-cell genome sequencing: current state of the science. Nat Rev Genet 2016;17:175-188.

21. **Dobie R, Wilson-Kanamori JR,** Henderson BEP, Smith JR, Matchett KP, Portman JR, Wallenborg K, et al. Single-Cell Transcriptomics Uncovers Zonation of Function in the Mesenchyme during Liver Fibrosis. Cell Rep 2019;29:1832-1847 e1838.

22. **Van de Sande B, Flerin C, Davie K,** De Waegeneer M, Hulselmans G, Aibar S, Seurinck R, et al. A scalable SCENIC workflow for single-cell gene regulatory network analysis. Nat Protoc 2020;15:2247-2276.

23. Aibar S, Gonzalez-Blas CB, Moerman T, Huynh-Thu VA, Imrichova H, Hulselmans G, Rambow F, et al. SCENIC: single-cell regulatory network inference and clustering. Nat Methods 2017;14:1083-1086.

24. Liu X, Xu J, Rosenthal S, Zhang LJ, McCubbin R, Meshgin N, Shang L, et al. Identification of Lineage-Specific Transcription Factors That Prevent Activation of Hepatic Stellate Cells and Promote Fibrosis Resolution. Gastroenterology 2020.

25. Adachi M, Osawa Y, Uchinami H, Kitamura T, Accili D, Brenner DA. The forkhead transcription factor FoxO1 regulates proliferation and transdifferentiation of hepatic stellate cells. Gastroenterology 2007;132:1434-1446.

26. Marcher AB, Bendixen SM, Terkelsen MK, Hohmann SS, Hansen MH, Larsen BD, Mandrup S, et al. Transcriptional regulation of Hepatic Stellate Cell activation in NASH. Sci Rep 2019;9:2324.

27. Katsumata LW, Miyajima A, Itoh T. Portal fibroblasts marked by the surface antigen Thy1 contribute to fibrosis in mouse models of cholestatic liver injury. Hepatol Commun 2017;1:198-214.

28. Wells RG. The portal fibroblast: not just a poor man's stellate cell. Gastroenterology 2014;147:41-47.

29. Hall KC, Bernier SG, Jacobson S, Liu G, Zhang PY, Sarno R, Catanzano V, et al. sGC stimulator praliciguat suppresses stellate cell fibrotic transformation and inhibits fibrosis and inflammation in models of NASH. Proc Natl Acad Sci U S A 2019;116:11057-11062.

30. Schwabl P, Brusilovskaya K, Supper P, Bauer D, Konigshofer P, Riedl F, Hayden H, et al. The soluble guanylate cyclase stimulator riociguat reduces fibrogenesis and portal pressure in cirrhotic rats. Sci Rep 2018;8:9372.

31. Knorr A, Hirth-Dietrich C, Alonso-Alija C, Harter M, Hahn M, Keim Y, Wunder F, et al. Nitric oxide-independent activation of soluble guanylate cyclase by BAY 60-2770 in experimental liver fibrosis. Arzneimittelforschung 2008;58:71-80.

32. Flores-Costa R, Alcaraz-Quiles J, Titos E, Lopez-Vicario C, Casulleras M, Duran-Guell M, Rius B, et al. The soluble guanylate cyclase stimulator IW-1973 prevents inflammation and fibrosis in experimental non-alcoholic steatohepatitis. Br J Pharmacol 2018;175:953-967.

33. **Evgenov OV, Pacher P, Schmidt PM, Hasko G, Schmidt HH, Stasch JP.** NO-independent stimulators and activators of soluble guanylate cyclase: discovery and therapeutic potential. Nat Rev Drug Discov 2006;5:755-768.

34. **Mannaerts I, Leite SB,** Verhulst S, Claerhout S, Eysackers N, Thoen LF, Hoorens A, et al. The Hippo pathway effector YAP controls mouse hepatic stellate cell activation. J Hepatol 2015;63:679-688.

35. **Mirolo M, Fabbri M, Sironi M,** Vecchi A, Guglielmotti A, Mangano G, Biondi G, et al. Impact of the anti-inflammatory agent bindarit on the chemokinome: selective inhibition of the monocyte chemotactic proteins. Eur Cytokine Netw 2008;19:119-122.

36. Seki E, de Minicis S, Inokuchi S, Taura K, Miyai K, van Rooijen N, Schwabe RF, et al. CCR2 promotes hepatic fibrosis in mice. Hepatology 2009;50:185-197.

37. Sandbo N, Lau A, Kach J, Ngam C, Yau D, Dulin NO. Delayed stress fiber formation mediates pulmonary myofibroblast differentiation in response to TGF-beta. Am J Physiol Lung Cell Mol Physiol 2011;301:L656-666.

38. Thannickal VJ, Lee DY, White ES, Cui Z, Larios JM, Chacon R, Horowitz JC, et al. Myofibroblast differentiation by transforming growth factor-beta1 is dependent on cell adhesion and integrin signaling via focal adhesion kinase. J Biol Chem 2003;278:12384-12389.

39. Chen W, Yang A, Jia J, Popov YV, Schuppan D, You H. Lysyl Oxidase (LOX) Family Members: Rationale and Their Potential as Therapeutic Targets for Liver Fibrosis. Hepatology 2020;72:729-741.

Author names in bold designate shared co-first authorship.

Figure 1.

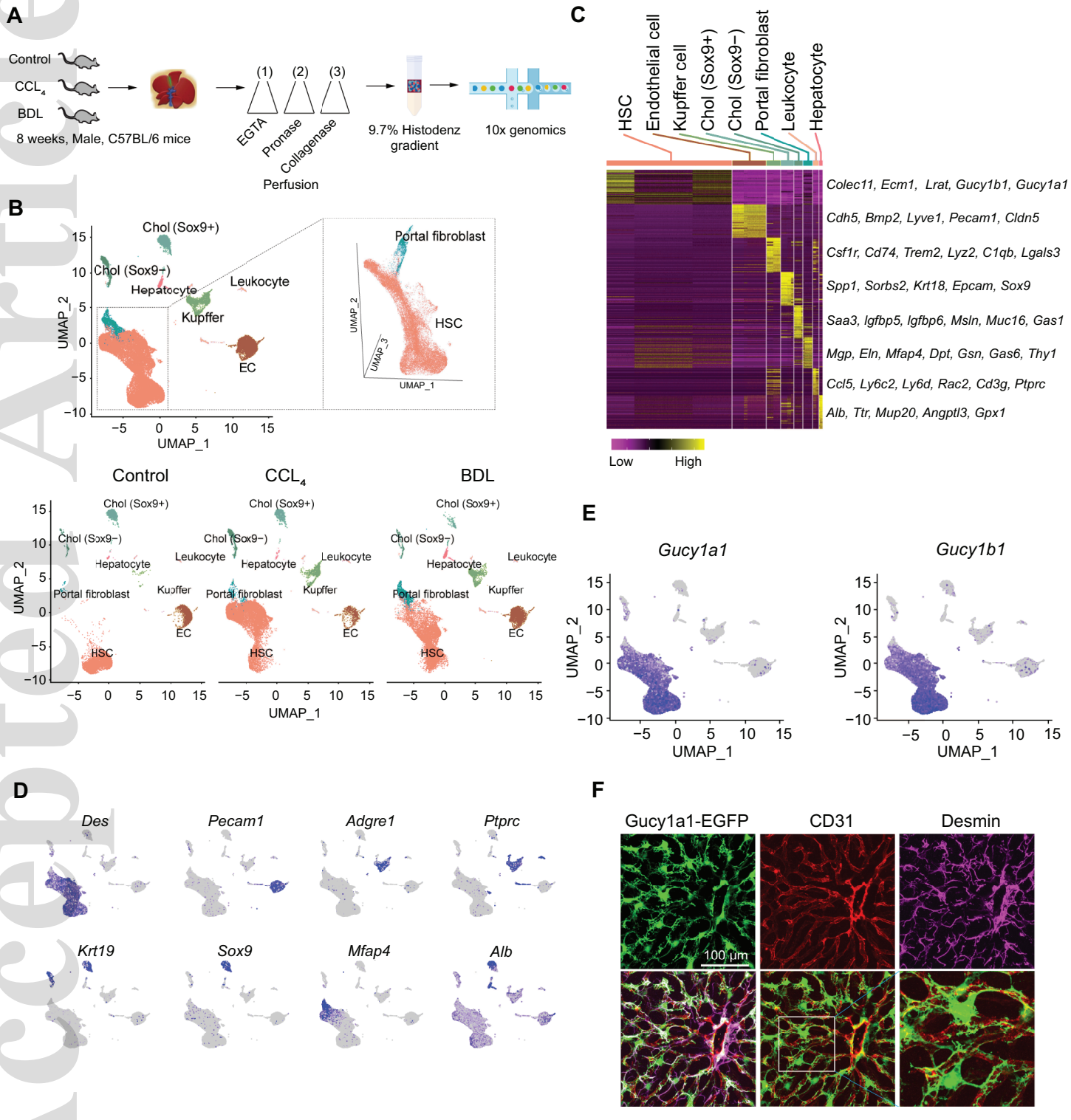

hep_31987_f1.eps

Figure 2.

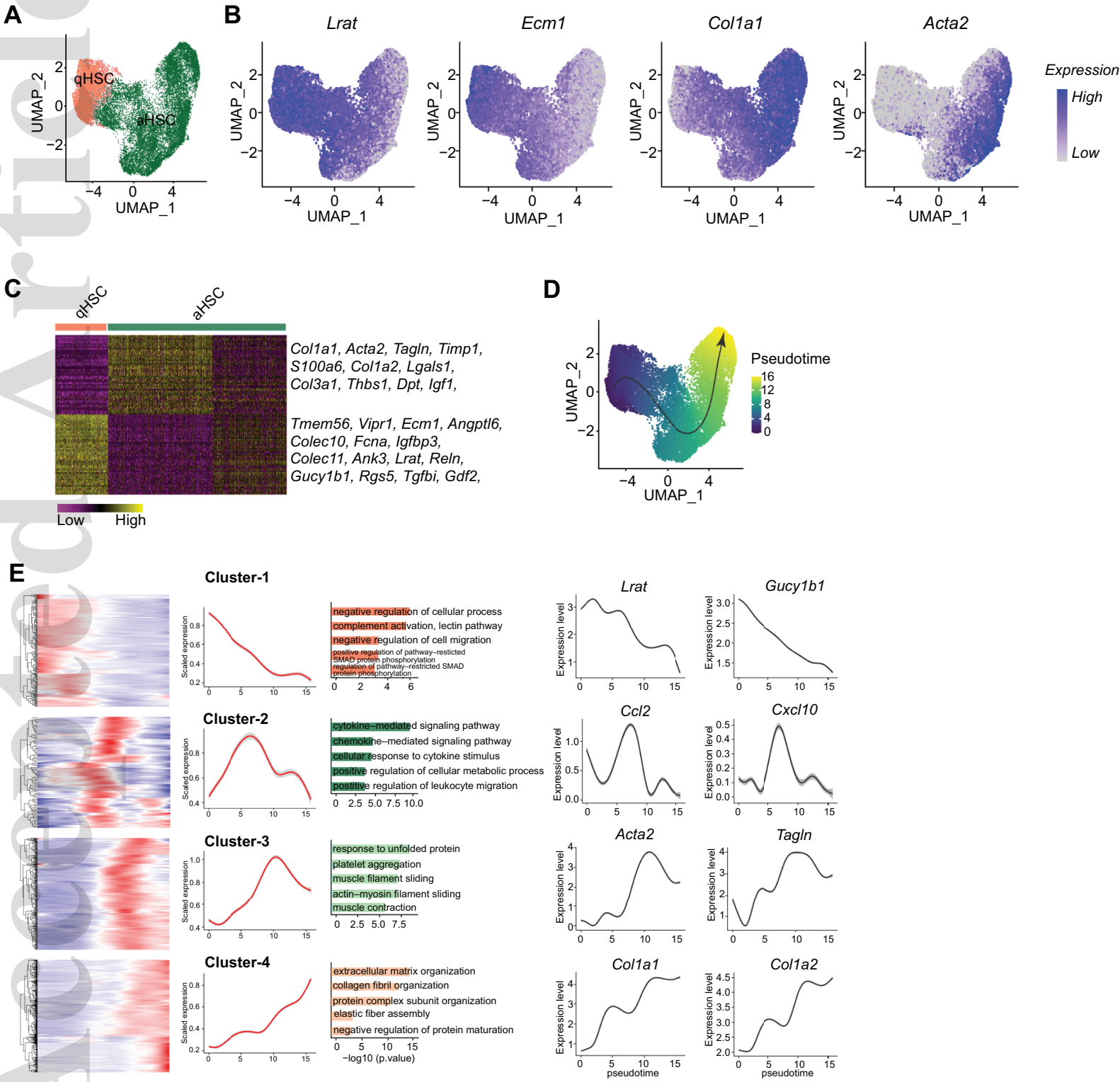

hep_31987_f2.eps

Figure 3.

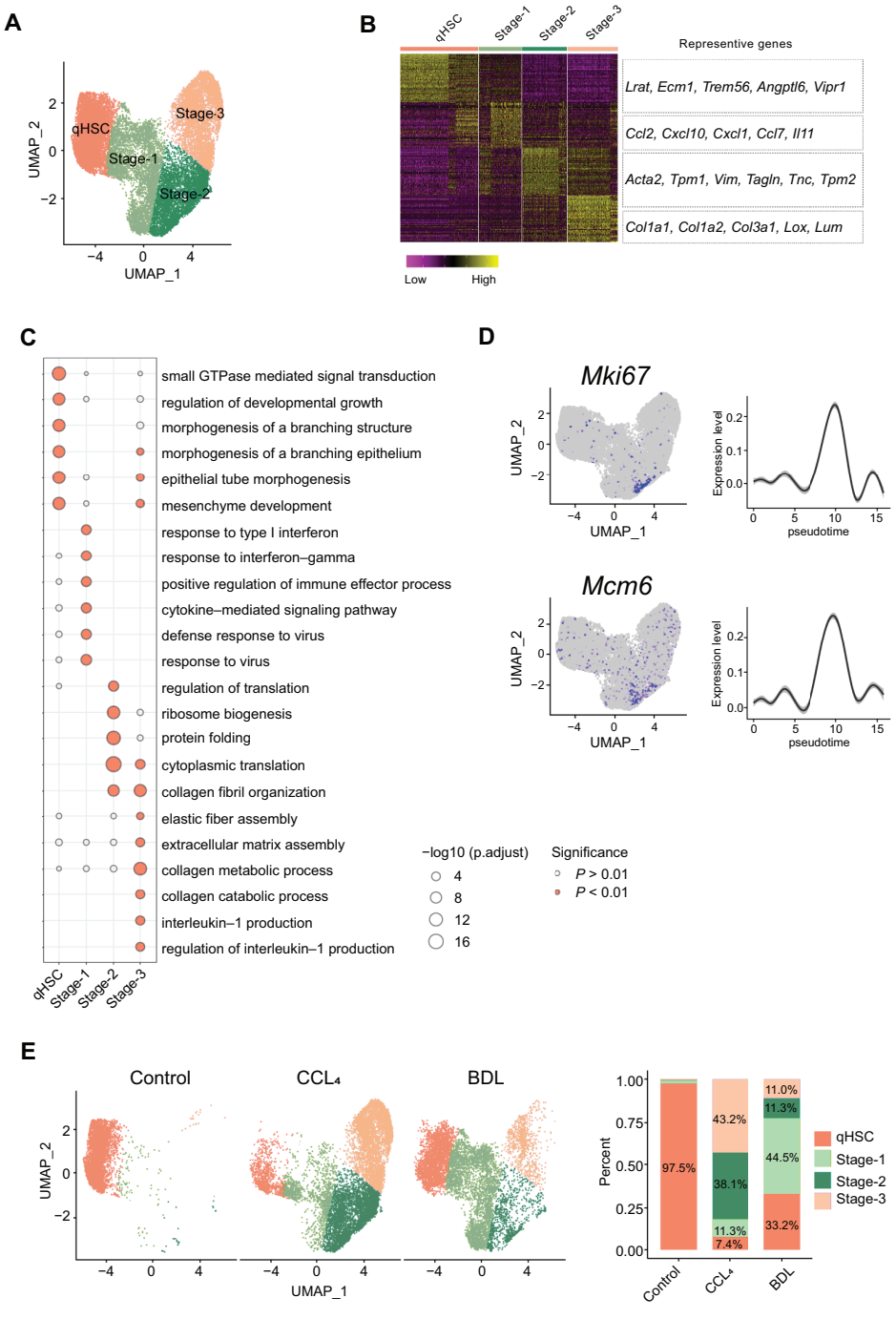

Figure 4.

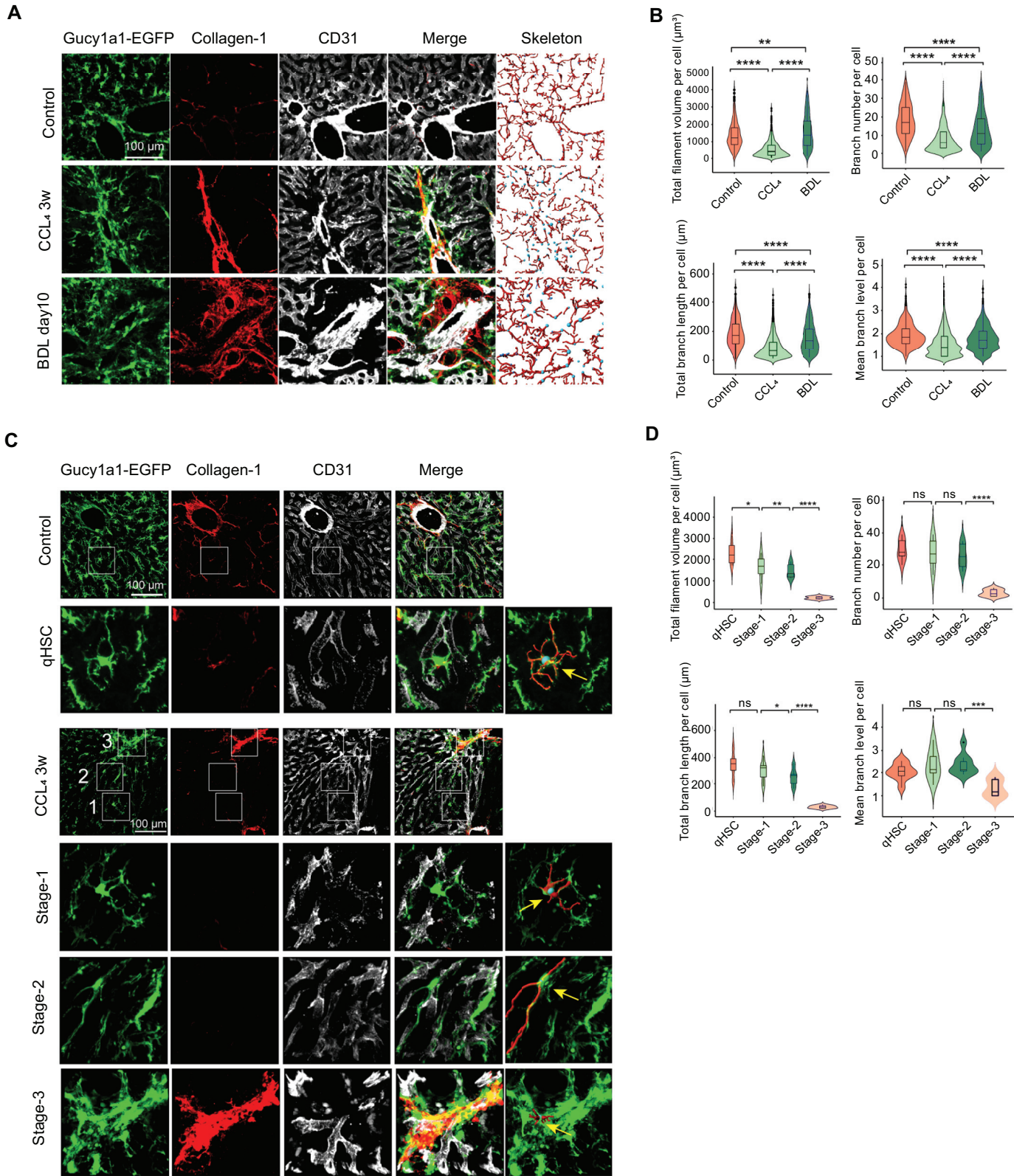
A
Gucy1a1-EGFP
Collagen-1
CD31
Merge
Skeleton
Control
CCL4 3w
BDL day10
100 μm
B
Total filament volume per cell (μm³)
Branch number per cell
Total branch length per cell (μm)
Mean branch level per cell
Control
CCL4
BDL
C
Gucy1a1-EGFP
Collagen-1
CD31
Merge
Control
qHSC
CCL4 3w
Stage-1
Stage-2
Stage-3
100 μm
D
Total filament volume per cell (μm³)
Branch number per cell
Total branch length per cell (μm)
Mean branch level per cell
qHSC
Stage-1
Stage-2
Stage-3
ns

Figure 5.

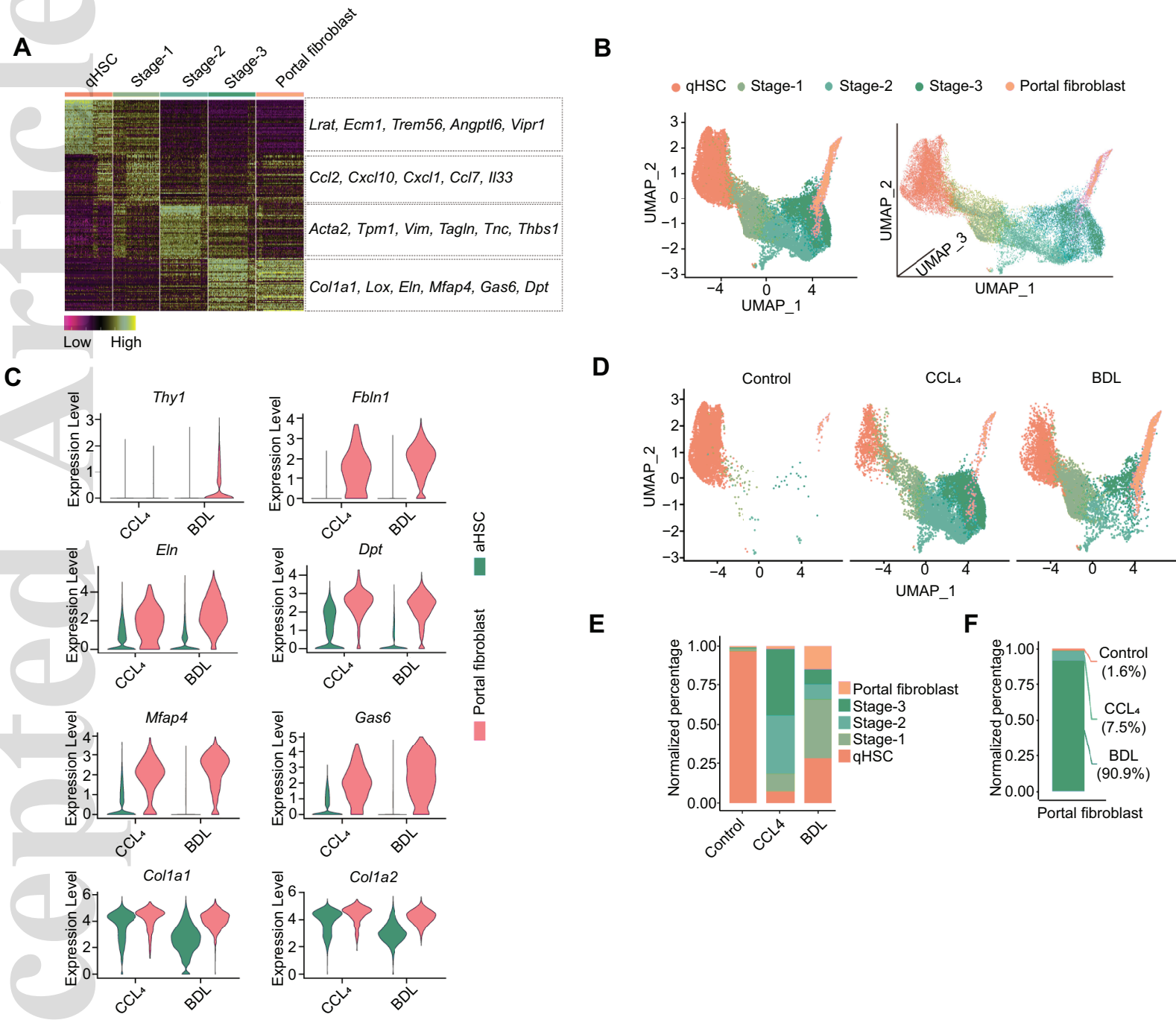

hep_31987_f5.eps

Figure 6.

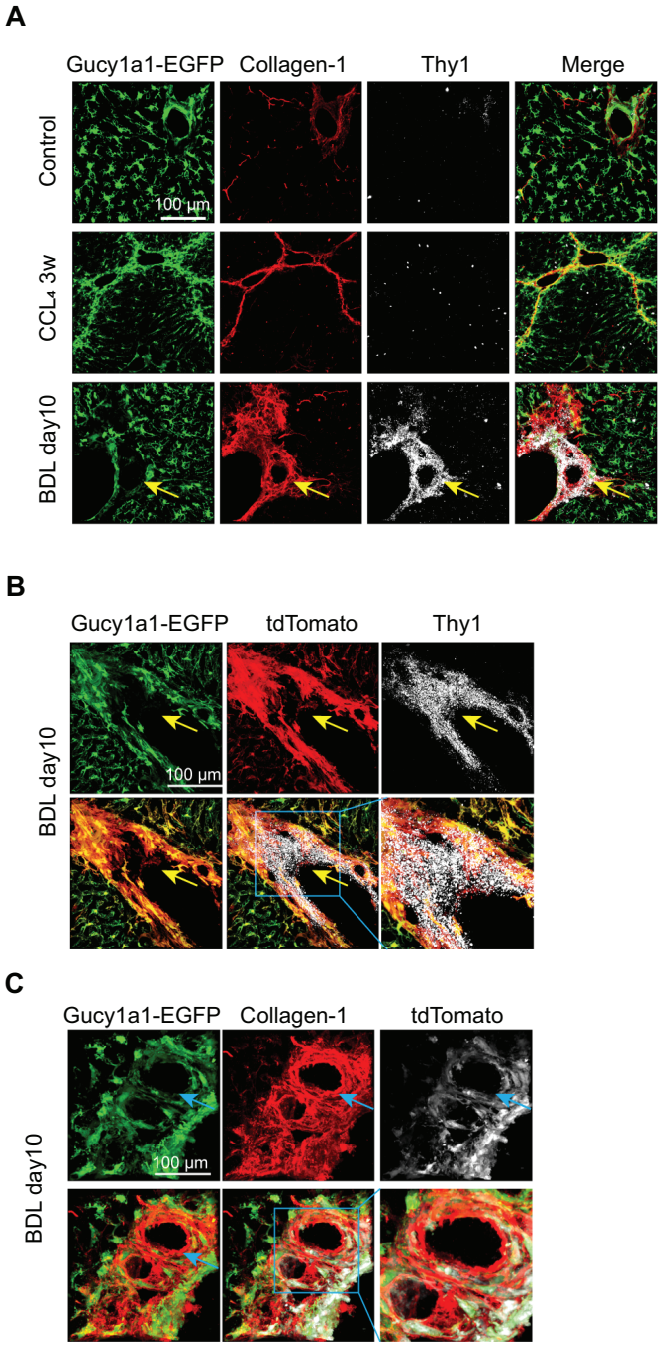

Figure 7.

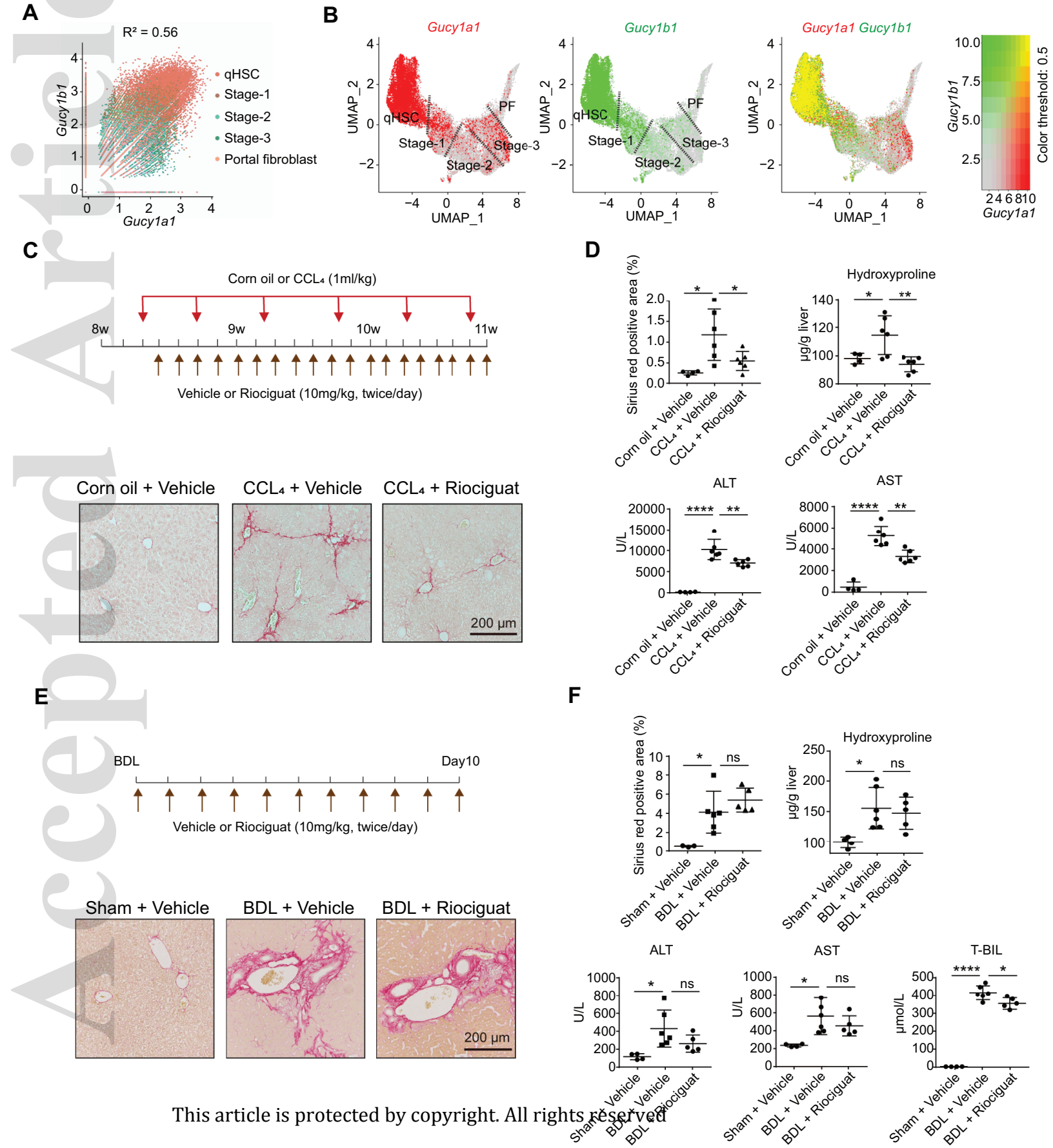

hep_31987_f7.eps